PERGAMON

International Journal of Solids and Structures 38 (2001) 8753–8772

INTERNATIONAL JOURNAL OF SOLIDS and STRUCTURES

www.elsevier.com/locate/ijsolstr

Spectral element technique for efficient parameter identification of layered media Part II: Inverse calculation

R. Al-Khoury, C. Kasbergen, A. Scarpas *, J. Blaauwendraad

Section of Structural Mechanics, Faculty of Civil Engineering and Geosciences, Delft University of Technology, Stevinweg 1, 2628 CN, Delft, Netherlands

Received 1 September 2000; in revised form 28 March 2001

Abstract

In Part I of this series of articles a forward model was presented for the simulation of wave propagation in a multi-layer system by means of the spectral element method. In the current article and, on the basis of the forward model, a procedure is presented for inverse calculation of the system parameters. The proposed procedure is based on iterative comparisons of measured versus theoretically determined system transfer functions. The performance of three minimization algorithms; factored Secant update, modified Levenberg–Marquardt and Powell hybrid for solving the resulting system of nonlinear equations is evaluated. For the problem under consideration, the Powell hybrid algorithm exhibits better stability and convergence characteristics. As an application, the inverse procedure is utilized for the determination of pavement layer moduli and thicknesses via the use of the falling weight deflectometer (FWD) test. The calculations show that the developed procedure is accurate and computationally efficient. As a result of these calculations, modifications to the standard practice of FWD measurements and instrumentation are suggested. © 2001 Elsevier Science Ltd. All rights reserved.

Keywords: Spectral element; Parameter identification; Backcalculation; Minimization; Falling weight deflectometer

1. Introduction

In Part I of this series of articles (Al-Khoury et al., 2001) the forward calculation of wave propagation in multi-layered systems due to transient loads was presented. Detailed mathematical derivation, implementation and verification of an axi-symmetric layer spectral element and a half-space spectral element were discussed. It was shown that because of the computational efficiency and robustness of the spectral element method (Doyle, 1997), it constitutes a practical tool for utilization in iterative schemes for parameter identification purposes.

* Corresponding author. Tel.: +31-15-278-4017; fax: +31-15-278-5767.
E-mail address: a.scarpas@ct.tudelft.nl (A. Scarpas).

0020-7683/01/$ - see front matter © 2001 Elsevier Science Ltd. All rights reserved.
PII: S0020-7683(01)00109-3

The computational efficiency is gained by the ability of the method to described wave propagation in a layer exactly. Hence, one element is sufficient to describe a whole layer. For a multi-layer system, the assemblage of layers is done by the use of the conventional finite element method. Consequently the size of the mesh of a layered system is only as large as the number of the layers involved. This reduces the computational requirements significantly.

The robustness of the method, on the other hand, is attributed to the series summation over the spatial domain. The series solution is made possible by assuming that the structure has a finite "remote" boundary (in the radial direction) at $r = R$ where waves vanish. This alleviates the inconvenience of the numerical implementation of infinite integration involved in solving wave propagation in structures with infinite boundaries.

In the present article (Part II of this series), a procedure for parameter identification of layered systems based on the spectral element method is presented. The procedure begins with the estimation of system transfer functions (also referred to as frequency response functions) from measured input/output data. On the basis of the formulations presented in Part I, the theoretical transfer functions are determined. Parameter identification is then performed by means of iterative comparison of measured versus theoretically determined transfer functions. This procedure results to a system of nonlinear equations whose variables represent the system parameters that are to be identified. Solving such system of equations requires minimization techniques.

In order to optimize the computational efficiency of the overall methodology, several minimization algorithms were evaluated in terms of their performance and stability in solving the resulting set of nonlinear equations of the problem under consideration.

As it is shown in this article, the combination of the spectral element method with an efficient minimization algorithm results to an elegant methodology for parameter identification of pavement layers via the use of the falling weight deflectometer (FWD) test.

2. Review of the falling weight deflectometer test

For roads and airfields the FWD test is a widely used non-destructive dynamic test for evaluation of pavement bearing capacity and for establishment of maintenance strategies for road networks.

The FWD instrument consists of a large mass that is dropped from a certain height onto a set of rubber buffers mounted to a 300 mm circular foot-plate (Van Gurp, 1995). The resulting force is measured by a load cell based at the plate center. Deflection sensors are used to record the vertical displacements at the surface at various radial distances from the loading center. Usually four to nine sensors are used to measure the displacements. The first is always mounted at the center of the foot-plate, while the rest are positioned at various distances (up to 2.5 m) from the center.

By varying the mass of the falling weight or the drop height or both, the impulse load can be varied between 30 and 110 kN, for the regular FWD types, and 30 and 250 kN for those used for airfields. Different FWD instruments produce different load pulse duration ranging between 20 and 60 ms. Typical FWD load pulse and surface deflections at different sensors positions are shown in Fig. 1 (Van Gurp, 1995).

In most of the currently used methodologies for FWD test data analyses, only maximum values of the load pulse and deflections are considered. Even though these maxima occur at different times from sensor to sensor, they are utilized to delineate an equivalent static "deflection bowl". Obviously ignoring the dynamic nature of the test introduces several flaws to the interpretation of test results.

The dynamic nature of the test has been taken into account in the backcalculation procedures developed by, among others, Magnuson et al. (1991) and Uzan (1994). Most of these procedures are based on the Kausel and Roesset (1981) type multi-layer model for the forward analysis and some general purpose minimization techniques, such as quasi-Newton, direct search or least square methods for parameter

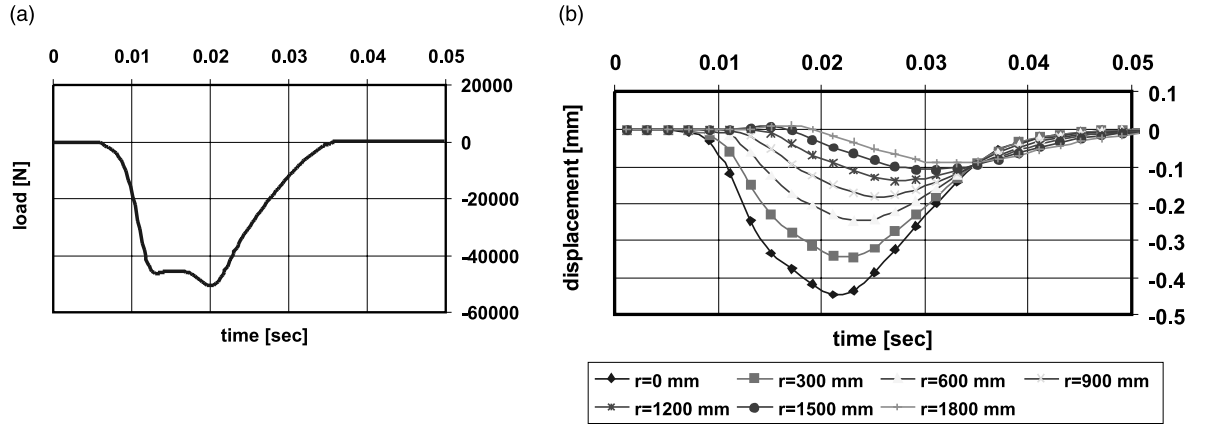

Fig. 1. Typical FWD (a) load pulse, and (b) surface vertical displacements.

identification. As was shown in Part I, whereas the Kausel–Roesset techniques are numerically suitable for forward calculations, they become computationally expensive when utilized in iterative schemes for solving inverse problems.

In the following a procedure for parameter identification of layered systems is presented. The special case of FWD test of pavement structures is emphasized.

3. A procedure for parameter identification of layered systems

Parameter identification of an engineering system entails determination of the system characteristics (structural geometry and/or material properties) from a given input force and an output response. For linear systems, the response function $w(t)$, at any location, is related to the impulse force function $P(t)$ by the convolution integral:

$$w(t) = \int_0^t G(t-\tau)P(\tau)\mathrm{d}\tau \tag{1}$$

in which $G(t-\tau)$ represents the characteristic function of the system, called the impulse response function. Alternatively, by applying the time-convolution theorem (Brigham, 1988), the time domain convolution of Eq. (1) can be replaced by simple algebraic multiplication in the frequency domain as

$$\hat{w}(\omega_n) = \hat{G}(\omega_n)\hat{P}(\omega_n) \tag{2}$$

in which ω_n is the angular frequency and the "hat" indicates the frequency domain formulation. $\hat{w}(\omega_n)$, $\hat{G}(\omega_n)$ and $\hat{P}(\omega_n)$ are the Fourier transforms of their time counterparts expressed as

$$\hat{w}(\omega_n) = \sum_{m=0}^{N-1} w(t)\mathrm{e}^{-\mathrm{i}\omega_n t_m}, \qquad \hat{G}(\omega_n) = \sum_{m=0}^{N-1} G(t)\mathrm{e}^{-\mathrm{i}\omega_n t_m}, \qquad \hat{P}(\omega_n) = \sum_{m=0}^{N-1} P(t)\mathrm{e}^{-\mathrm{i}\omega_n t_m}$$

respectively, in which m is the number of data samples and N is the sample at Nyquist frequency. $\hat{w}(\omega_n)$ may represent any physically observable quantity such as displacements, velocities or accelerations in any direction and $\hat{P}(\omega_n)$ may be any sort of excitation such as impulse, impact etc. The function $\hat{G}(\omega_n)$ is called the transfer function and characterizes the system in the frequency domain.

The transfer function of a system can be evaluated experimentally and characterized theoretically. In the followings, details of the spectral analysis of the measured and computed data and the mathematical formulation of their relationships are presented.

3.1. Analysis of measured data

When a linear system with impulse response functions $G_{sj}(t)$ is subjected to a series of measurable actions $P_j(t)$, $j = 1 \ldots J$, it produces some measurable output $w_s(t)$, which can be measured at some system locations $s = 1 \ldots S$. By applying Fourier transformation, Eq. (2) can be generalized to

$$\begin{Bmatrix} \hat{w}_1(\omega_n) \\ \hat{w}_2(\omega_n) \\ \vdots \\ \hat{w}_S(\omega_n) \end{Bmatrix} = \begin{bmatrix} \hat{G}_{11}(\omega_n) & \hat{G}_{12}(\omega_n) & \cdots & \hat{G}_{1J}(\omega_n) \\ \hat{G}_{21}(\omega_n) & \hat{G}_{22}(\omega_n) & \cdots & \hat{G}_{2J}(\omega_n) \\ \vdots & \vdots & \vdots & \vdots \\ \hat{G}_{S1}(\omega_n) & \hat{G}_{S2}(\omega_n) & \cdots & \hat{G}_{SJ}(\omega_n) \end{bmatrix} \begin{Bmatrix} \hat{P}_1(\omega_n) \\ \hat{P}_2(\omega_n) \\ \vdots \\ \hat{P}_J(\omega_n) \end{Bmatrix} \tag{3}$$

Eq. (3) is a matrix presentation of the spectral relationships for a typical multiple-input/multiple-output (MI/MO) system (Bendat and Piersol, 1993).

For the special case of the FWD test, a single force is applied at surface location $j = 1$ and vertical displacements are measured at a series of sensor locations $1 \ldots S$ positioned at some distances away from the loading center. For such a system, Eq. (3) reduces to

$$\begin{Bmatrix} \hat{w}_1(\omega_n) \\ \hat{w}_2(\omega_n) \\ \vdots \\ \hat{w}_S(\omega_n) \end{Bmatrix} = \begin{Bmatrix} \hat{G}_1(\omega_n) \\ \hat{G}_2(\omega_n) \\ \vdots \\ \hat{G}_S(\omega_n) \end{Bmatrix} \hat{P}_1(\omega_n) \tag{4}$$

Eq. (4) represents the spectral relationships for a typical single-input/multiple-output (SI/MO) system. In such a system, the transfer function at any location s, for a given frequency ω_n, can be determined by

$$\hat{G}_s(\omega_n) = \frac{\hat{w}_s(\omega_n)}{\hat{P}_1(\omega_n)} \tag{5}$$

Eq. (5) is in effect a complex division between the displacement and the force spectra. As an application, Eq. (5) is utilized for calculation of the transfer functions of the pavement system whose measurement results are shown in Fig. 1. The amplitude of the real and imaginary parts of the transfer functions at radial distances $r = 0$ and 1500 mm are shown in Fig. 2. In this, the fast Fourier transformation (FFT) was utilized for the transformation of the load pulse data, Fig. 1a, and the corresponding sensor displacement data, Fig. 1b. A sampling rate $\Delta t = 0.0002$ s for 2048 sampling points was used in the FFT process.

Examination of the experimental frequency response data for a complicated system, such as a multi-layered system, is not always apparent mainly in the complex space. Usually, in signal analysis, magnitudes and phase angles are presented in logarithmic scales. Fig. 3 shows the logarithmic presentation of the magnitudes of the transfer functions of Fig. 2. It can be seen that at low frequencies the transfer function is nearly flat. This indicates that the system is not sensitive to the frequency changes in this range of frequencies. At higher frequencies, however, the response can be distinguished at each frequency.

3.2. Analysis of computed data

In Part I it was shown that for an axi-symmetric layer (with cylindrical coordinates r, θ, z) the force–displacement relationship, in the frequency domain, can be expressed as

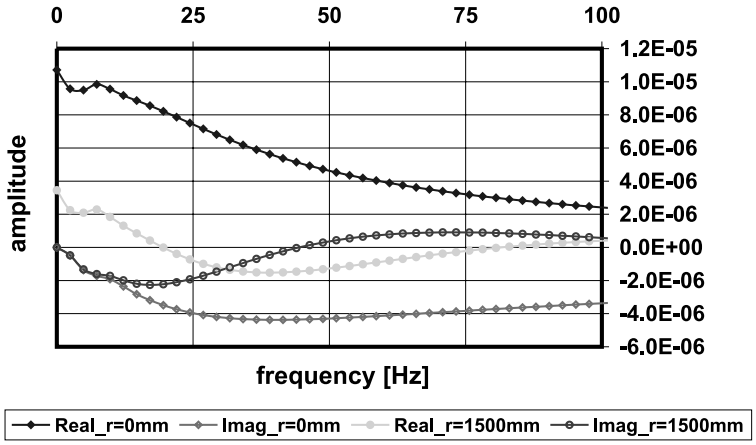

Fig. 2. Transfer function spectrums at $r = 0$ and 1500 mm.

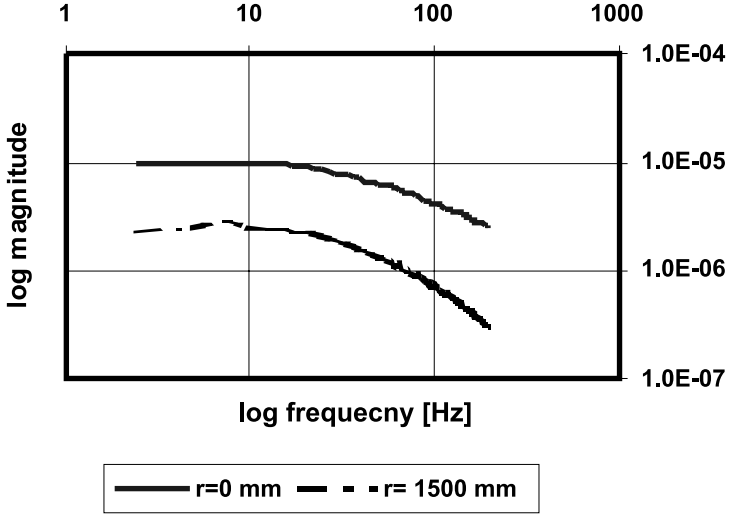

Fig. 3. The transfer function spectrums in log–log scale.

$$\begin{Bmatrix} \hat{w}(r,z,\omega_n) \\ \hat{u}(r,z,\omega_n) \end{Bmatrix} = \sum_m \hat{P}_{mn}\hat{G}(k_m,\omega_n,z)\begin{Bmatrix} J_0(k_m r) \\ J_1(k_m r) \end{Bmatrix} \tag{6}$$

in which $\hat{w}(r,z,\omega_n)$ and $\hat{u}(r,z,\omega_n)$ are the vertical and horizontal displacements respectively, $\hat{P}_{mn}$ denotes the force pulse, $\hat{G}(k_m,\omega_n,z)$ represents the transfer function of the layer, J_0 and J_1 are the Bessel functions of the first kind of order 0 and 1 respectively, k_m is the wave number and ω_n is the angular frequency. Summation over M wave numbers constructs the vibration modes of the system. Even though it is not shown in Eq. (6), it is worth mentioning here that, summation over N frequencies reconstructs the time response of the system.

For a multi-layer system, on the basis of the spectral element method, the force–displacement relationship can be obtained as

$$[\hat{\mathbf{K}}(k_m,\omega_n)]\{\hat{\mathbf{D}}(r,z,\omega_n)\} = \{\hat{\mathbf{P}}(k_m,\omega_n)\} \tag{7}$$

in which $[\hat{\mathbf{K}}(k_m,\omega_n)]$ represents the stiffness matrix of the system, $\{\hat{\mathbf{D}}(r,z,\omega_n)\}$ denotes the nodal displacement vector and $\{\hat{\mathbf{P}}(k_m,\omega_n)\}$ represents the external force vector. Details of the formulation of the stiffness matrix of a spectral layer element and a spectral half-space element and their implementation are presented in Part I.

By complex inversion of Eq. (7), the displacements in a multi-layer system, for a given mode m and frequency n, can be determined by

$$\{\hat{\mathbf{D}}(r,z,\omega_n)\} = [\hat{\mathbf{H}}(k_m,\omega_n)]\{\hat{\mathbf{P}}_{mn}(k_m,\omega_n)\} \tag{8}$$

in which the $[\hat{\mathbf{H}}(k_m,\omega_n)]$ is the matrix inverse of $[\hat{\mathbf{K}}(k_m,\omega_n)]$. Apparently $[\hat{\mathbf{H}}(k_m,\omega_n)]$ represents the transfer function of the multi-layer system.

For the case of the FWD test where a single load is applied at the surface, the force–displacement relationship can be expressed as

$$\begin{Bmatrix} \hat{w}_{1mn} \\ \hat{u}_{1mn} \\ \vdots \\ \hat{u}_{Dmn} \end{Bmatrix} = \begin{Bmatrix} \hat{H}_{11}(k_m,\omega_n) \\ \hat{H}_{21}(k_m,\omega_n) \\ \vdots \\ \hat{H}_{2D}(k_m,\omega_n) \end{Bmatrix} \hat{P}_{1mn} \tag{9}$$

in which subscripts fd in the vector $\{\hat{H}_{fd}\}$ denote the number of the degree of freedom and the node number respectively (at each node $d = 1 \ldots D$ there are two degrees of freedom, $f = 1$ for the vertical and $f = 2$ for the radial). Comparing Eq. (9) with Eq. (4) reveals that $\hat{H}_{fd}$ is the transfer function for the degree of freedom f at the element node d. A schematic of the locations at which $\hat{H}_{fd}$ is evaluated, is shown in Fig. 4. Also, the locations are shown where the measured transfer function $\hat{G}_s$ is evaluated by means of Eq. (4).

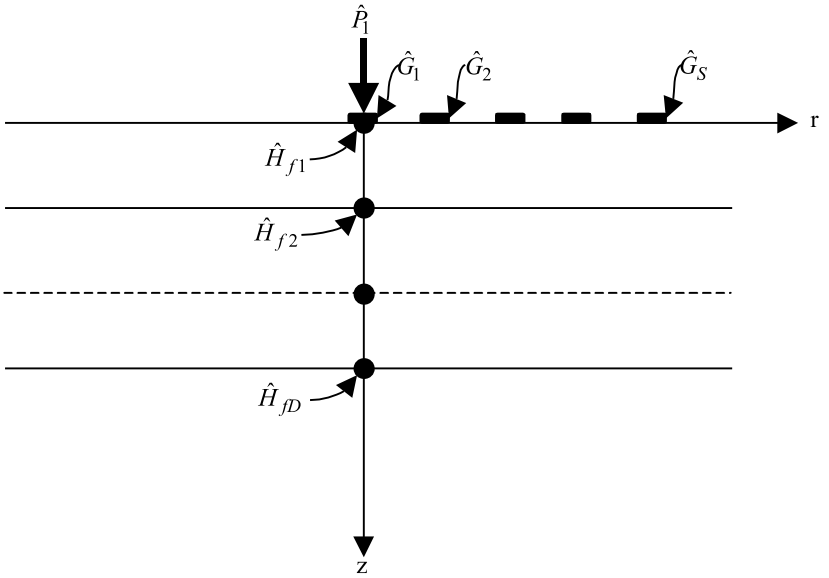

Fig. 4. Locations of the measured and computed system transfer functions.

The FWD load pulse $\hat{P}_{1mn}$ is expressed as

$$\hat{P}_{1mn} \equiv \frac{1}{A}\hat{F}_m(a)\hat{F}_n[F(t)] \tag{10}$$

in which A is the loading area, $\hat{F}_m(a)$ is the Fourier–Bessel coefficients of the spatial distribution of the FWD load with radius a and $\hat{F}_n[F(t)]$ denotes the fast Fourier coefficients of its time variation $F(t)$.

Because in the FWD test, only vertical displacements are measured, therefore, only vertical displacements at sensor locations are calculated by means of Eq. (9). By substituting Eq. (10) into Eq. (9) and, as indicated in Eq. (6), the overall vertical displacement at any node d, in the frequency domain, can be computed by summing over all m vibration modes as

$$\hat{w}_{dmn} = \frac{1}{A}\sum_m \hat{F}_m\hat{F}_n\hat{H}_{1d}(k_m, \omega_n, z) \tag{11}$$

Once the vertical displacement at the node is determined, the vertical displacement at any radial position r_i along the layer surface where the node is located, Fig. 4, can be calculated by

$$\hat{w}^i_{dmn} = \frac{1}{A}\sum_m \hat{F}_m\hat{F}_n\hat{H}_{1d}(k_m, \omega_n, z)J_0(k_m r_i) \tag{12}$$

3.3. The system objective function

Due to the superposition principle of the spectral analysis, it is convenient to deal with a unit load and its corresponding displacements. Thus, by letting $\hat{P}_1(\omega_n) = 1$ in Eq. (5), the measured vertical displacement per unit load, at sensor s, becomes

$$\hat{w}_s(\omega_n) = \hat{G}_s(\omega_n) \tag{13}$$

In the same way, by letting $\hat{F}_n = 1$ in Eq. (12), the theoretical vertical displacement, at any radial position r_i, reduces to

$$\hat{w}^i_{dmn} = \frac{1}{A}\sum_m \hat{F}_m\hat{H}_{1d}(k_m, \omega_n, z)J_0(k_m r_i) \tag{14}$$

The core of the proposed procedure lies in imposing sharing information between measured and theoretical displacements, Fig. 4, as a result of a unit load. This means that measured displacements at any sensor location s, calculated from Eq. (13), are equated to those calculated by Eq. (14) for $d = 1$ (the node directly under the load, Fig. 4) and $i = s$, so that:

$$\left\{\frac{1}{A}\sum_m \hat{F}_m\hat{H}_{11}(k_m, \omega_n, z)J_0(k_m r_s)\right\}_{\text{theoretical}} = \left\{\hat{G}_s(\omega_n)\right\}_{\text{measured}} \tag{15}$$

Evaluating Eq. (15) at S sensor locations results to a system of complex nonlinear equations. Eq. (15) can be written in terms of the differences of its scalar magnitudes as

$$q_s(\mathbf{x}) = \left|\frac{1}{A}\sum_m \hat{F}_m\hat{H}_{11}(k_m, \omega_n, z)J_0(k_m r_s)\right|_{\text{theoretical}} - \left|\hat{G}_s(\omega_n)\right|_{\text{measured}} \tag{16}$$

in which $\mathbf{x}$ represents the vector of the unknown variables such as layer elastic modulus, thickness, etc. Eq. (16) represents the objective function of a pavement structure subjected to an FWD load pulse.

The computer implementation of the objective function, Eq. (16), was performed on the basis of the formulations, which were derived in Part I. To recall, the evaluation of k_m is done by discretizing, analytically, the vibration modes in the radial direction. This was done by assuming that the wave vanishes at a distance R far away from the source. Mathematically, this means that at $r = R$, $J_0(kR) = 0$, which can only be satisfied at the positive roots α_m of the J_0 function. This implies $kR = \alpha_m$, thus $k = k_m = \alpha_m/R$.

$\hat{F}_m$ for a cylindrical shape with radius a and amplitude 1 can be derived analytically (Kreyszig, 1999) as

$$\hat{F}_m = \frac{2a}{\alpha_m R J_1^2(\alpha_m)} J_1\left(\frac{\alpha_m}{R} a\right) \tag{17}$$

$\hat{H}_{11}(k_m, \omega_n, z)$ is determined on the basis of the inverse of the spectral structural stiffness matrix $[\hat{K}(k_m, \omega_n)]$ as the term corresponding to the vertical degree of freedom $f = 1$ at node $d = 1$, Fig. 4.

The calculation of these factors, k_m, $\hat{F}_m$ and $\hat{H}_{11}(k_m, \omega_n, z)$, is repeated m times and, after their substitution in Eq. (14), the results are summed. Summation over m constructs the theoretical displacement per unit load in the frequency domain. Then, by substituting the result into Eq. (16), the objective function of the system can readily be constructed. Solution of Eq. (16) is discussed in the following section.

From the above discussion it can be deduced that the primary benefit of the utilization of the spectral element method for the inverse calculation manifests itself in three features. The first is that the spectral formulation of the stiffness matrix $[\hat{K}(k_m, \omega_n)]$ leads naturally to the construction of the system objective function. The second is that $[\hat{K}(k_m, \omega_n)]$ is symmetric, banded and concise (the number of the elements are equal to the number of the layers involved). Therefore its inversion requires less computational effort, rendering thus the iterative schemes more efficient. The third is the algebraic summation over m wave numbers, which avoids the numerical integration over infinity. This feature adds robustness to the computations.

4. Minimization techniques for solving the system objective function

The derivation of the objective function, Eq. (16), has lead inevitably to a system of nonlinear equations. Solving such a system requires the use of non-linear optimization methods. Nonlinear optimization is concerned with methods for locating, for this case, the least value of the objective function of any number of independent variables. The least value problem is called minimization.

Over the years many minimization techniques for solving multi-dimensional nonlinear equations have been developed. However, until now there is not yet a general technique that can be used to solve a wide range of problems. In this research work, three methods have been adopted for comparative study. (Gill et al. (1981) provide an important overview on strategies for selecting minimization methods suitable for problems at hand.) The adopted methods are:

1. factored secant update method for solving a non-constrained system of nonlinear simultaneous equations with a finite-difference Jacobian,
2. modified Levenberg–Marquardt algorithm for solving a constrained over determined nonlinear least squares problems with a finite-difference Jacobian and
3. modified Powell hybrid algorithm for solving a non-constrained system of nonlinear simultaneous equations with a finite-difference Jacobian.

In the next section, comparisons between the performance of the three methods are presented. For completeness, some brief outline of the main features of each algorithm is given in the Appendix A.

5. Performance of the minimization algorithms

The proposed procedure was implemented in the software package LAMDA (layered media dynamic analysis). LAMDA was utilized to examine the performance of the minimization algorithms in terms of stability and rate of convergence. Stability relates to the ability of an algorithm to converge to a minimum value $\tilde{x}_i$ regardless of the starting point (Scales, 1985). The rate of convergence refers to the performance of the algorithm at each iteration and the total number of iterations necessary for convergence. It depends on the characteristics of the algorithm itself and/or the objective function.

The Euclidean norm defined as

$$\|\mathbf{x}-\tilde{\mathbf{x}}\|_2=\left\{\sum_{i=1}^{n}(x_i-\tilde{x}_i)^2\right\}^{1/2} \tag{18}$$

in which $\mathbf{x}$ is the variable vector and $\tilde{\mathbf{x}}$ is the known minimum, is used as a criterion.

At this stage of investigation and for the sake of verifying the mathematical derivations and computer implementation of the developed parameter identification procedure, only computed (not contaminated) data was utilized. For this reason, FWD forward analyses for some representative pavement with known properties were performed by use of the forward model (presented in Part I). Vertical displacements at typical FWD sensor locations were output. Then, the FWD force data together with the displacements data were utilized as input to the inverse model to calculate back the layer parameters. These parameters were Young's moduli and layer thicknesses.

In principle, backcalculation of layer parameters can be done at each frequency. However, in order to thoroughly evaluate the performance of the developed procedure, inverse calculations at a range of frequencies were performed. In the following, four cases varying between a relatively simple to a relatively difficult one were examined.

5.1. Case 1: Identification of material moduli of a typical pavement

A pavement structure consisting of an asphalt layer ($E=1000$ MPa and $h=150$ mm), a subbase layer ($E=200$ MPa and $h=250$ mm) and subgrade layer ($E=25$ MPa and $h=\infty$) was simulated as a typical case for FWD analysis. The computed vertical displacements obtained from the forward model were utilized as input for inverse calculations.

All three minimization algorithms were utilized for backcalculation of the material Young's moduli of the three layers. The initial guess for the moduli were: $E_{\text{asphalt}}=200$ MPa, $E_{\text{subbase}}=40$ MPa and $E_{\text{subgrade}}=5$ MPa, which represents 20% of the correct values.

The inverse calculations were performed at frequencies ranging between 0 and 80 Hz. The stability of the minimization algorithms, at some selected frequencies, are shown in Table 1. It can be seen that all algorithms have converged to a minimum with varying norm accuracy: (to give an impression about the norm values of Table 1, norm of $2.84\text{E}-01$ refers to back calculated value of $E_{\text{asphalt}}=1000.11$ MPa, $E_{\text{subbase}}=199.43$ MPa and $E_{\text{subgrade}}=25.09$ MPa, and norm of $6.81\text{E}+01$ refers to $E_{\text{asphalt}}=933.21$ MPa, $E_{\text{subbase}}=212.52$ MPa and $E_{\text{subgrade}}=19.88$ MPa).

Fig. 5 compares the performance of the algorithms for the whole range of frequencies. The following can be noticed:

1. All algorithms did not converge at frequencies lower than 8 Hz. As was mentioned in Section 2 and was shown in Fig. 3, the system transfer functions were independent of the frequency variation at the low frequency range. This can be attributed to the fact that at these frequencies, the corresponding harmonic load duration may approach that of a static loading.

Table 1
Stability performance

Frequency (Hz)	$\|\mathbf{x}-\tilde{\mathbf{x}}\|_2$		
	Powell	Secant	Levenberg–Marquardt
11.7	5.22E − 02	2.84E − 01	8.95E − 06
15.6	3.83E − 06	9.99E − 01	9.83E − 06
27.3	3.38E − 03	4.50E + 00	1.24E − 07
37.1	3.39E − 03	5.45E + 00	3.83E − 07
46.9	4.84E − 04	2.16E + 01	6.17E − 08
56.6	3.21E − 03	1.38E + 01	1.80E − 08
76.2	6.79E − 02	6.81E + 01	6.06E − 09

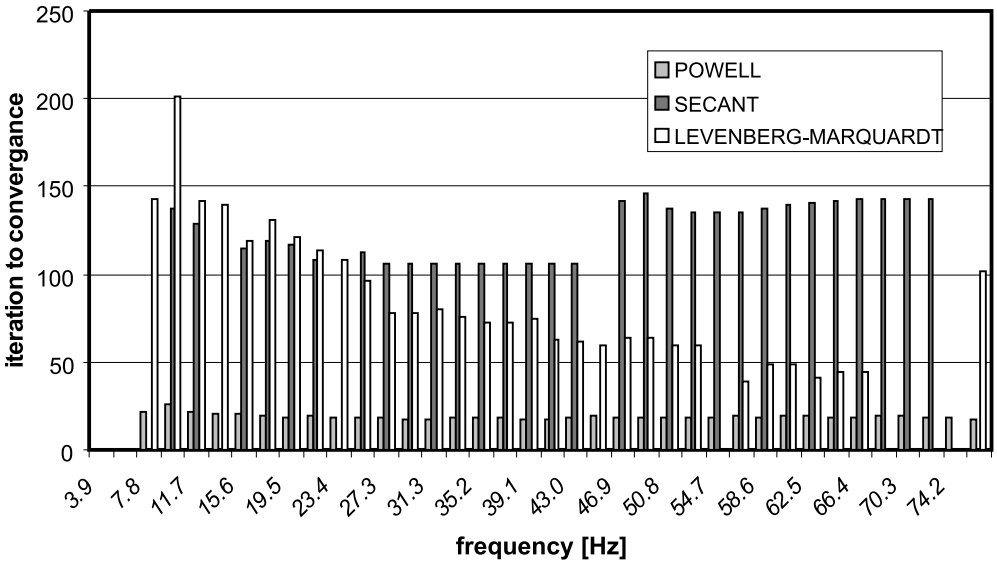

Fig. 5. Stability performance for Case 1.

2. Powell's algorithm converged at all frequencies beyond 8 Hz. However, the Secant and the Levenberg–Marquardt did not converge at some of them. Both required good initial guess for convergence.
3. Powell's algorithm converged to the minimum with less than 20 iterations, while Secant required more than 100 iterations and Levenberg–Marquardt required about 70. It is worth mentioning that each iteration requires less than a second on a Pentium II processor.

To examine the convergence rate of the three algorithms, Table 2 lists the performance of the algorithms at one of the frequencies (37.1 Hz) during some selected iterations. Also, Fig. 6 shows the performance of the algorithms during the whole iteration process. From these, the following can be observed:

1. The descend of Powell to the minimum is steep at all iterations.
2. The descend of Levenberg–Marquardt is steep at some iterations. However, as described in the appendix, after each relatively steep descent, the Levenberg–Marquardt algorithm uses Gauss–Newton to evaluate the objective function over a very small region with little reduction of its value. In case of Powell,

Table 2
Convergence rate performance

Iteration number	$\|\mathbf{x}-\tilde{\mathbf{x}}\|_2$		
	Powell	Secant	Levenberg–Marquardt
0	302.25	302.25	302.25
5	188.18	250.82	298.20
10	39.61	160.01	298.20
17	0.001	100.43	298.18
50		21.51	0.22
68		9.91	0.0001
105		2.01	

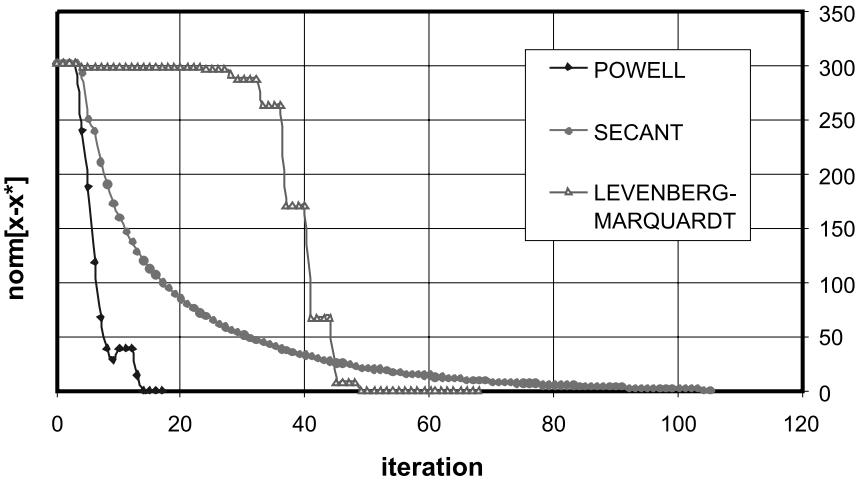

Fig. 6. Convergence rate for Case 1.

even after a steep descent, if $\mathbf{p}_k$ (Eq. (A.7)) is within the trust region, it continues to use the same descending algorithm until it otherwise violates the trust region criterion.

3. The descend of secant is gradual as expected.

From the above it can be inferred that, for the problem under consideration, the convergence rate of Powell is superior to the other two.

5.2. Case 2: Identification of material moduli and layer thicknesses of a typical pavement

The same profile as in Case 1 was utilized, but in this case it was assumed that the unknowns included also the layer thicknesses. Same initial guesses of material moduli as in Case 1 were used. The initial guess for the thickness was 200 mm for the top two layers.

During examination of the stability of the algorithms, same trend of convergence as that of Table 1 was observed and therefore not included here. Fig. 7 shows the performance of the three algorithms at a range of frequencies. The following can be observed:

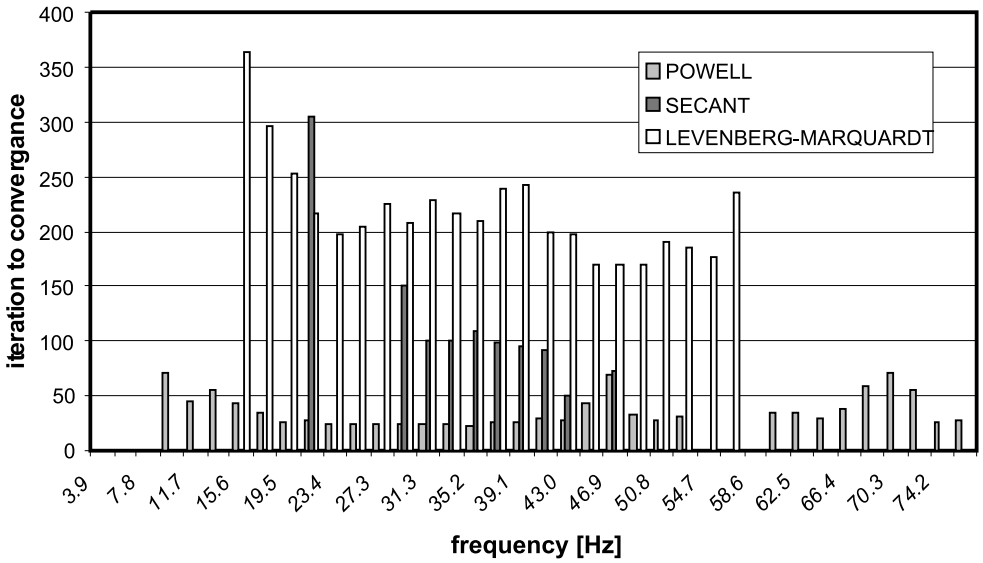

Fig. 7. Stability performance for Case 2.

1. At low frequencies all algorithm did not converge for the reason mentioned in Case 1.
2. Powell converged at all frequencies (beyond 10 Hz) except at frequencies between 55 and 58 Hz, at which it diverged from attaining the correct minimum. By examining the condition numbers of the transfer function matrix at the minimum values, it occurred that the condition numbers at this range of frequencies are approximately equal to those at slightly lower or slightly higher frequencies. It seems that there is no apparent mathematical reason for divergence at this particular range of frequencies. A possible reason may be the inevitable loss of some information during the discrete Fourier transformation, which may have lead to a mismatch between the forcing frequency and the corresponding displacements. Good initial guess was necessary for convergence.

   In practice, in order to avoid this type of numerical ambiguities, it is recommended that backcalculation is performed at more than one frequency. Considering the computational efficiency of the whole procedure, this is not regarded as a serious drawback.
3. The secant algorithm converged at only 10 frequencies out of 41 used. Even though Levenberg–Marquardt performed better than the Secant, it converged for fewer cases compared with Powell.
4. Powell converged extremely faster than the other two algorithms.

Fig. 8 compares the convergence rates of the three algorithms. Same conclusions can be drawn as for Case 1 with the exception that in Case 2 Levenberg–Marquardt did not exhibit steep descent towards the minimum.

As in Case 1, for the problem under consideration, the performance of Powell was superior to those of the other two algorithms.

5.3. Case 3: Identification of material moduli of a pavement with cement stabilized subbase

A pavement consisted of an asphalt layer ($E = 2000$ MPa and $h = 150$ mm), a subbase ($E = 5000$ MPa and $h = 250$ mm) and a subgrade ($E = 25$ MPa and $h = \infty$) was simulated. In engineering practice this combination is important for two reasons. First, for pavements on a weak subsoil, a stiff subbase layer is

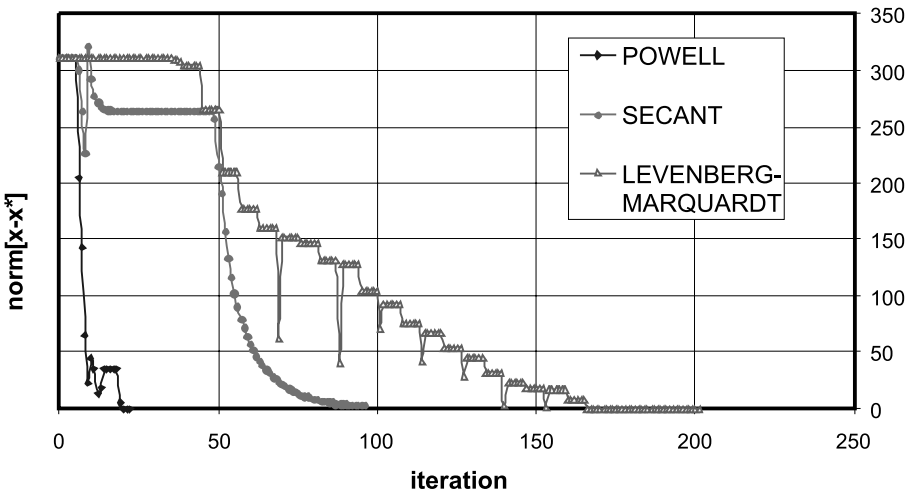

Fig. 8. Convergence rate for Case 2.

needed on top of the soil. Second, classical backcalculation procedures have been known to exhibit numerical instability when the ratio of the layer's stiffnesses become high.

All three algorithms were utilized for backcalculation of the material Young's modulus. The initial guess for the Young's moduli were: $E_{\text{asphalt}} = 400$ MPa, $E_{\text{subbase}} = 1000$ MPa and $E_{\text{subgrade}} = 5$ MPa, which represent 20% of the correct values.

Fig. 9 compares the performance of the algorithms for the whole range of frequencies. It can be seen that Powell's algorithm had managed to converge at all frequencies beyond 10 Hz, while the other two had failed in some of them.

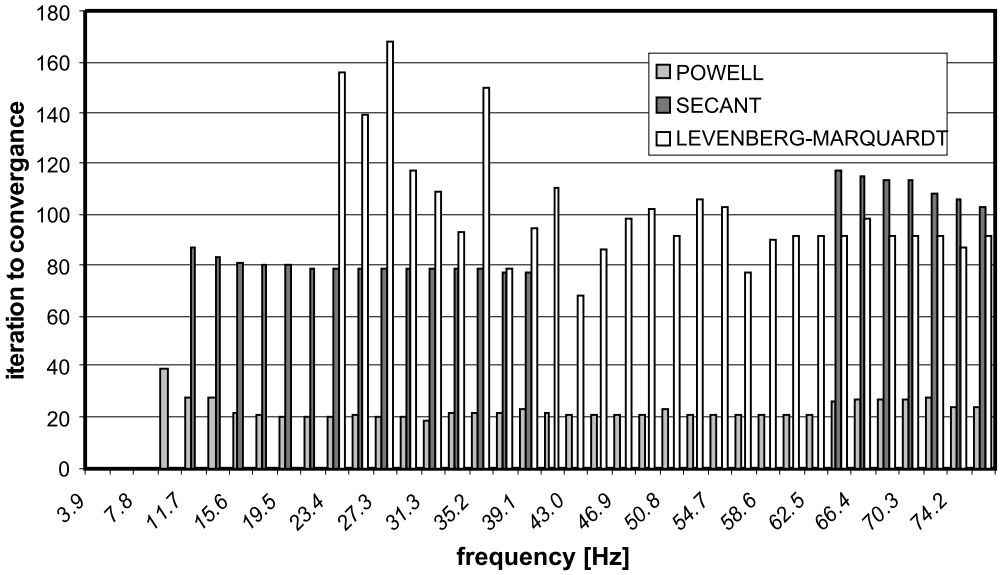

Fig. 9. Stability performance for Case 3.

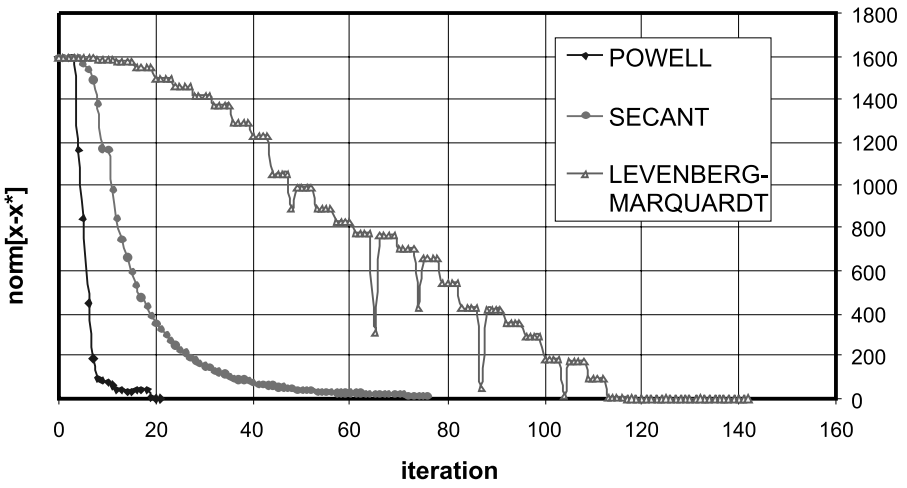

Fig. 10. Convergence performance for Case 3.

Fig. 10 compares the convergence rate of the three algorithms during the iteration process. It can be seen that Powell exhibits the steepest descend to the minimum.

From Figs. 9 and 10 it is obvious that the performance of Powell's algorithm is, again, superior in terms of stability and rate of convergence compared with the other two.

5.4. Case 4: Identification of material moduli and layer thicknesses of a pavement with cement stabilized subbase (uniqueness issues)

The same profile as in Case 3 was used with the assumption that, in addition to the moduli, the layer thicknesses were also unknown. In this particular case the number of unknowns and the associated complications brought about by the stiffness ratios and their distribution may result in a non-unique solution. To tackle this problem a modification has been applied to the system objective function in order to extract more information so as to come up with a unique solution. The uniqueness issue is described in this case study.

Because of the better performance of Powell's method in the previous cases, it was utilized solely in this case. At first, initial guesses representing 20% of the correct values were attempted. The results were poor. This indicates that the objective function may exhibit clustered local minima. Usually, for such a function, the solver is not able to distinguish between the global and the local minimum.

A second attempt was done by increasing the initial guess to represent about 50% of the actual values. Inverse analysis was performed for a range of frequencies. The predictions of Powell, at three different frequencies (62, 66 and 78 Hz), together with the actual values, the initial guesses and the output results, are shown in Table 3. It can be seen that three solutions were obtained with high convergence accuracy, as expressed by $\chi = \left(\sum_{s=1}^{S} q_s(\mathbf{x})^2\right)/S$, in which S is the number of variables. (χ is the convergence criterion used by the algorithm.)

The low χ indicates that all solutions in Table 3 are mathematically correct. To illustrate this, forward analysis was conducted using the parameters obtained from the first solution (at 62 Hz) and the third solution (at 78 Hz). Fig. 11 presents the analysis results for both cases, from which it can be seen that, for all practical purposes, the results are identical.

These identical responses in the vertical direction obtained from different combinations of E-moduli and layer thicknesses might give an impression that there is no unique solution to the problem. However,

Table 3
Powell predictions at three different frequencies

Parameter	Actual value	Initial guess	Estimated value		
			62 Hz $\chi = 9.49\text{E}-29$	66 Hz $\chi = 1.68\text{E}-25$	78 Hz $\chi = 1.94\text{E}-23$
E_{asphalt} (MPa)	2000	1000	1999.99	1776.36	1543.77
E_{subbase} (MPa)	5000	2500	4999.99	4565.54	4566.81
E_{subgrade} (MPa)	25	15	25.00	25.20	25.25
h_{asphalt} (mm)	150	200	149.99	112.08	88.48
h_{subbase} (mm)	250	200	250.00	292.02	313.28

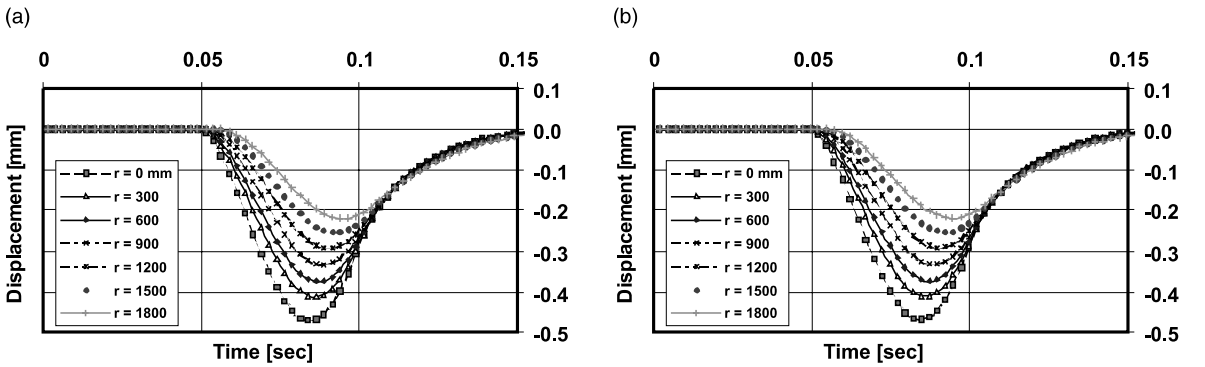

Fig. 11. Forward analysis, (a) parameters of frequency = 62 Hz, (b) parameters of frequency = 78 Hz.

convergence to a unique and correct solution can be enhanced if additional aspects of the dynamic response of the pavement can be taken into account and, in particular, the radial displacements at the surface of the pavement structure.

As shown in Fig. 12, by means of the forward model, the surface radial displacements were computed for the pavement structure whose layer parameters are presented in Table 3 (at 62 and 78 Hz) at stations located at 1200, 1500 and 1800 mm from the load center. Despite the aforementioned similarities in the vertical response of these pavements, differences in the radial response can be seen from Fig. 12.

To investigate the significance of utilizing the radial displacements for the enhancement of the uniqueness of the solution, the system objective function was modified to include both vertical and radial displacements. The radial displacement at the surface at sensor position $i = s$, for a unit load, is calculated as

$$\hat{u}^s_{1mn} = \frac{1}{A}\sum_m \hat{F}_m \hat{H}_{21}(k_m, \omega_n, z) J_1(k_m r_s) \tag{19}$$

in which $\hat{H}_{21}(k_m, \omega_n, z)$ is the transfer function corresponding to the radial displacement $f = 2$ at node $d = 1$ (see Eq. (9) and Fig. 4).

Eq. (19) constitutes a vector perpendicular to the vertical displacement vector $\hat{w}_{imn}$. The resultant magnitude of these two vectors was utilized to construct a new objective function as

$$q_s(\mathbf{x}) = \left\{\sqrt{|\hat{w}_{smn}|^2 + |\hat{u}_{smn}|^2}\right\}_{\text{theoretical}} - \left\{\sqrt{|\hat{w}_s(\omega_n)|^2 + |\hat{u}_s(\omega_n)|^2}\right\}_{\text{measured}} \tag{20}$$

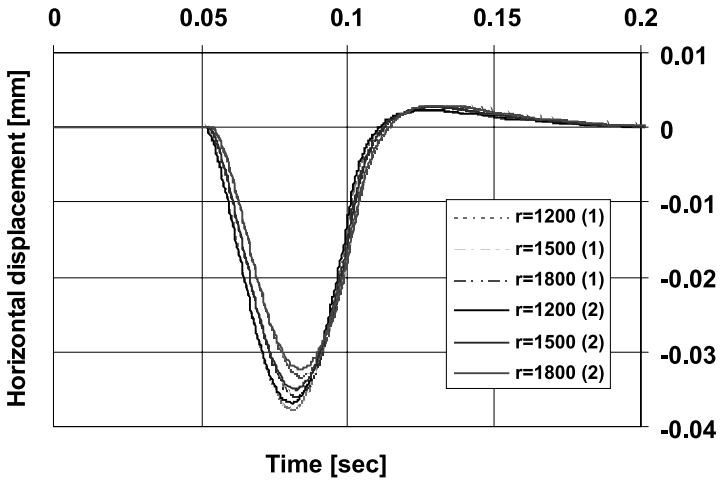

Fig. 12. Radial displacements for the two analyses.

Table 4
Inverse calculations with and without radial displacements

Displacement data	Sensor location	Inverse calculation results		
		Convergence to right solution	Convergence to other solution	Divergence
Vertical	Near field	3	14	3
Vertical + radial	Near field	16	4	0
Vertical + radial	Far field	20	0	0

at each sensor location s. This objective function was used for re-evaluation of the layer parameters of this case study. New analyses were performed and compared with the previous one:

1. vertical and radial displacements data of the near field sensors (0, 300, 600, 900, 1200 mm) were utilized, and
2. vertical and radial displacement data including the far field sensors (0, 900, 1200, 1500, 1800 mm) were utilized.

The analyses were conducted for a range of 20 frequencies. Table 4 shows the inverse calculation results for all analyses. It can be seen that the addition of more data to the process, convergence to the correct solution was improved. The uniqueness in the third analysis was more pronounced than in the second one because the far field sensors (1200, 1500 and 1800 mm, Fig. 12) exhibit large differences in radial displacements.

This finding is of practical significance for road engineering because, currently non-uniqueness raises doubts about the validity of the back calculated layer parameters.

6. Conclusions

In this series of articles the development of a complete methodology for parameter identification of layered systems had been presented. Both a forward model and an inverse model were developed with the

aim of better accuracy, robustness and computational efficiency. This aim was achieved by utilization of the spectral element method for the development of the forward model and use of minimization techniques that were able to switch between different convergence strategies for the development of the inverse model. The following overall conclusions can be drawn:

1. The axi-symmetric spectral layer element and the half-space element developed and implemented in this research project were shown to be able to accurately simulate wave propagation in layered media due to transient loads.
2. Because waves are described exactly in the spectral element method, one element is adequate to describe a whole layer. Consequently, the size of the mesh of a layered structure is only as large as the number of the layers involved. This reduces the computational requirements dramatically. For inverse calculation each iteration takes around 1 s in a typical Pentium II processor.
3. The double summation approach of the spectral element avoids the inconvenience of the numerical evaluation of the integration between zero and infinity involved in the spatial domain. This introduces robustness to the computation.
4. The formulation of the spectral elements leads automatically to the determination of the theoretical transfer functions at any point in the structure. By relating the theoretical transfer functions with those obtained from the measurements, analytical objective function of the system can readily be constructed. General purposes minimization techniques can be utilized for solving the nonlinear set of equations resulting for the construction of the objective function. However, algorithms that are able to switch between different search direction strategies were shown to perform better. It was found that the performance of the Powell hybrid algorithm, for the cases under consideration, was superior to those of the factored Secant update and the modified Levenberg–Marquardt algorithms.
5. Inclusion of the horizontal displacements in the parameter identification procedure resulted to drastic improvements in convergence and uniqueness of the solution. For engineering purposes it is strongly recommended that, in the future, the measured data should also include horizontal displacements.

Acknowledgements

The research project is partially funded by the European Commission under the Standards, Measurements and Testing programme of the Fourth Framework under project name "SpecifiQ". The authors are grateful to the SpecifiQ project leader Dr. C. Van Gurp for the many discussions and insight he has provided in the course of the project.

Appendix A

A.1. Factored secant update algorithm

The factored secant update algorithm (Dennis and Schnabel, 1983) solves a system of nonlinear equations in a manner similar to that of Newton's methods but with Secant approximation to the Jacobians proposed by Broyden (1970). The algorithm solves

$$q_s(\mathbf{x}) = 0, \quad \text{with } q : R^s \to R^s \quad \text{and} \quad \mathbf{x} \in R^s \tag{A.1}$$

in which $q_s(\mathbf{x})$ represents the objective function, i.e. Eq. (16), to be solved from functions R^s into R^s, where s is the number of parameters. This means that s sensors are used to compute s parameters.

From a given $\mathbf{x}_k$ (initial guess) the algorithm solves the following minimization problem

$$\min_{\mathbf{p}_k \in R^s} \|q_s(\mathbf{x}_k) + J(\mathbf{x}_k)\mathbf{p}_k\|_2, \quad \text{so that} \quad \|\mathbf{p}_k\|_2 \leqslant \delta_c \tag{A.2}$$

from which $\mathbf{p}_k$, which represents the search direction vector, is calculated. $\| \ \|_2$ is the Euclidean norm, $J(\mathbf{x}_k)$ is the finite difference approximation to the Jacobian at $\mathbf{x}_k$, and δ_c is the trust region, which limits the size of $\mathbf{p}_k$.

Then, the next point $\mathbf{x}_{k+1} = \mathbf{x}_k + \mathbf{p}_k$ is calculated and used as the current point $\mathbf{x}_k$. If the new $q_s(\mathbf{x}_k)$ satisfies the stopping criterion, it follows that the algorithm has attained the minimum successfully. Otherwise, δ_c is adjusted and the finite difference Jacobian $J(\mathbf{x}_{k+1})$ is updated according to Broyden's update formula

$$J(\mathbf{x}_{k+1}) = J(\mathbf{x}_k) + \mathbf{Q}_k^B \tag{A.3}$$

in which

$$\mathbf{Q}_k^B = \frac{((q_s(\mathbf{x}_{k+1}) - q_s(\mathbf{x}_k)) - J(\mathbf{x}_k)\cdot\mathbf{p}_k)\mathbf{p}_k^{\mathrm{T}}}{\mathbf{p}_k^{\mathrm{T}}\cdot\mathbf{p}_k}.$$

The algorithm then continues by using the updated point $\mathbf{x}_{k+1} = \mathbf{x}_k + \mathbf{p}_k$ with the updated Jacobian $J(\mathbf{x}_{k+1})$ and repeats the process until the criterion is fulfilled.

A.2. Modified Levenberg–Marquardt algorithm

The Levenberg–Marquardt algorithm (Scales, 1985) solves nonlinear least-squares problems. It combines Newton's methods and the steepest descent method. The steepest descent is used to seek for sufficiently close estimates to the minimum point, from which Newton methods is used for the refinement of the results to match the stopping criterion.

The problem to be solved is constrained, which can be stated as

$$\min_{\mathbf{x}\in R^r} \frac{1}{2} q_s^{\mathrm{T}}(\mathbf{x}) q_s(\mathbf{x}) = \frac{1}{2}\sum_{s=1}^{S} f_s(\mathbf{x})^2, \quad \text{with } l \leqslant \mathbf{x} \leqslant u \tag{A.4}$$

where S is the number of sensors ($S \geqslant r$), r is the number of variables, $q_s(\mathbf{x})$ is the objective function, Eq. (16), to be minimized from functions R^r into R^S, and l and u are the bounds for $\mathbf{x}$.

The Levenberg–Marquardt method modifies the Guess–Newton formula

$$J^{\mathrm{T}}(\mathbf{x}_k)J(\mathbf{x}_k)\mathbf{p}_k = -J^{\mathrm{T}}(\mathbf{x}_k)q_s(\mathbf{x}_k) \tag{A.5}$$

to include a non-negative scalar μ_k called the Levenberg–Marquardt parameter:

$$(J^{\mathrm{T}}(\mathbf{x}_k)J(\mathbf{x}_k) + \mu_k\mathbf{I})\mathbf{p}_k = -J^{\mathrm{T}}(\mathbf{x}_k)q_s(\mathbf{x}_k) \tag{A.6}$$

in which $J(\mathbf{x}_k)$ is the finite difference approximation of the Jacobian at the point $\mathbf{x}_k$, $\mathbf{I}$ is the identity matrix of order r and $\mathbf{p}_k$ is the search direction. First, $\mathbf{p}_k$ is calculated from a given $\mathbf{x}_k$. For sufficiently large difference between $\mathbf{x}_k$ and the minimum $\tilde{\mathbf{x}}$ (large value of μ_k) $\mathbf{p}_k$ takes the steepest decent direction. Then the next point $\mathbf{x}_{k+1} = \mathbf{x}_k + \mathbf{p}_k$ is calculated and used as the current point $\mathbf{x}_k$. As $\mathbf{x}_k \to \tilde{\mathbf{x}}$ ($\mu_k \to 0$), the method adopts asymptotic rate of convergence of the Gauss–Newton method. If the new $q_s(\mathbf{x}_k)$ satisfies the stopping criterion, it follows that the algorithm has attained the minimum successfully. Otherwise, μ_k is adjusted by multiplying or dividing it by some scalar value and fed back to Eq. (A.6). Then the new equation is solved to obtain a new $\mathbf{p}_k$ and so on until convergence to the minimum occurs.

A.3. Powell hybrid algorithm

The Powell hybrid method (Scales, 1985) solves a system of nonlinear equations with no constraints. Powell's algorithm exhibits many similarities to the Levenberg–Marquardt algorithm mentioned above. As for Levenberg–Marquardt, Powell algorithm flips between quasi-Newton and steepest decent iteration techniques according to a step size criterion. The step size parameter Δ_k, which defines the region of trust (similar to δ_c in the secant method), is the factor used by the algorithm to decide upon the type of iteration.

One of the important differences between Powell's algorithm and the Levenberg–Marquardt algorithm is in the determination of the search direction $\mathbf{p}_k$. In the latter, at each iteration, $\mathbf{p}_k$ is calculated by solving Eq. (A.6). In Powell, however, the search direction $\mathbf{p}_k$ is first calculated by the quasi-Newton iteration:

$$J(\mathbf{x}_k)\mathbf{p}_k = -q_s(\mathbf{x}_k) \rightarrow \mathbf{p}_k = -H(\mathbf{x}_k)q_s(\mathbf{x}_k) \quad \text{so that} \quad \|\mathbf{p}_k\|_2 \leqslant \Delta_k \tag{A.7}$$

in which $q_s(\mathbf{x})$ is the objective function, Eq. (16), to be minimized, $J(\mathbf{x}_k)$ is the finite difference approximation of the Jacobian at the point $\mathbf{x}_k$, and $H(\mathbf{x}_k)$ is its inverse. Then it is checked whether the norm of $\mathbf{p}_k$ is smaller than a step size Δ_k or not. If it is smaller, this search direction is accepted and the next point will be $\mathbf{x}_{p+1} = \mathbf{x}_p + \mathbf{p}_k$. If not, a second criterion is tested, which is defined as

$$\alpha_k\|\mathbf{r}_k\| \geqslant \Delta_k \tag{A.8}$$

in which $\mathbf{r}_k = -J^{\mathrm{T}}(\mathbf{x}_k)q_s(\mathbf{x}_k)$ and

$$\boldsymbol{\alpha}_k = \frac{\|J^{\mathrm{T}}(\mathbf{x}_k)q_s(\mathbf{x}_k)\|^2}{\|J(\mathbf{x}_k)J^{\mathrm{T}}(\mathbf{x}_k)q_s(\mathbf{x}_k)\|^2}.$$

If this criterion is satisfied, the next point $\mathbf{x}_{k+1} = \mathbf{x}_k + \mathbf{p}_k$ will be calculated as a pure steepest decent, in which $\mathbf{p}_k = (\Delta_k/\|\mathbf{r}_k\|)\mathbf{r}_k$. If, however, both criteria fail, the new search direction $\mathbf{x}_{k+1} = \mathbf{x}_k + \mathbf{p}_k$ will be a hybrid between the quasi-Newton and the steepest descent, in which $\mathbf{p}_k = \beta_k q_s(\mathbf{x}_k) + (1-\beta_k)\boldsymbol{\alpha}_k\mathbf{r}_k$ and β_k is such that$\|\Delta\mathbf{x}_k\| = \Delta_k$.

Another important difference between the Powell algorithm and the Levenberg–Marquardt algorithm is that the latter calculates, at each iteration, the Jacobian matrix, while the former is updating it similar to that in the Secant method.

From above it can be noticed that the determination of $\mathbf{p}_k$ in Powell's algorithm requires less computational effort than that in the Levenberg–Marquardt algorithm.

The above three algorithms are provided by the IMSL package (IMSL, 1997).

References

Al-Khoury, R., Scarpas, A., Kasbergen, C., Blaauwendraad, J., 2001. Spectral element technique for efficient parameter identification of layered media. I. Forward calculation. Int. J. Solids Struct. 38, 1605–1623.

Bendat, J.S., Piersol, A.G., 1993. Engineering Applications of Correlation and Spectral Analysis. Wiley, New York.

Brigham, E.O., 1988. The Fast Fourier Transform and Its Applications. Prentice-Hall, Englewood Cliffs, NJ.

Broyden, C.G., 1970. The convergence of a class of double-rank minimization algorithms. J. Inst. Maths. Appl. 6, 76–90.

Dennis, J.E., Schnabel, R.B., 1983. Numerical Methods for Unconstrained Optimization and Nonlinear Equations. Prentice-Hall, Englewood Cliffs, NJ.

Doyle, J.F., 1997. Wave Propagation in Structures: Spectral Analysis Using Fast Discrete Fourier Transforms. Springer, New York.

Gill, P.E., Murray, W., Wright, M.H., 1981. Practical Optimization. Academic Press, New York.

IMSL, Fortran subroutine for mathematical applications. Math/Library, vols. 1 and 2, 1997. Visual Numerics, Inc.

Kausel, E., Roesset, J.M., 1981. Stiffness matrices for layered soils. Bull. Seism. Soc. Am. 71, 1743–1761.

Kreyszig, E., 1999. Advanced Engineering Mathematics. Wiley, New York.

Magnuson, A.H., Lytton, R.L., Briggs, R.C., 1991. Comparison of computer predictions and field data for dynamic analysis of falling weight deflectometer data. Transport. Res. Rec. 1293, 61–71.

Scales, L.E., 1985. Introduction to Non-Linear Optimization. Macmillan, New York.

Uzan, J., 1994. Dynamic linear back calculation of pavement material parameters. J. Transport. Engng. 120, 109–126.

Van Gurp, C., 1995. Characterization of seasonal influences on asphalt pavements with the use of falling weight deflectometers. Ph.D. Thesis. Technical University of Delft, CIP, Delft.